SCIENTIFIC REPORTS

OPEN

In vitro evaluation of the toxic effects of MgO nanostructure in Hela cell line

Received: 8 September 2017
Accepted: 6 March 2018
Published online: 15 March 2018

M. Waseem Akram[1], Muhammad Fakhar-e-Alam[1,2], M. Atif[3,4], Alvina Rafique Butt[5], Ali Asghar[6], Yasir Jamil[7], K. S. Alimgeer[8] & Zhiming M. Wang[1]

MgO is an attractive choice for carcinogenic cell destruction in photodynamic therapy, as confirmed by manifold analysis. The prime focus of the presented research is to investigate the toxicity caused by morphologically different MgO nanostructures obtained by annealing at various annealing temperatures. Smart (stimuli-responsive) MgO nanomaterials are a very promising class of nanomaterials, and their properties can be controlled by altering their size, morphology, or other relevant characteristics. The samples investigated here were grown by the co-precipitation technique. Toxicity-dependent parameters were assessed in a HeLa cell model after annealing the grown samples at 350 °C, 450 °C, and 550 °C. After the overall characterization, an analysis of toxicity caused by changes in the MgO nanostructure morphology was tested in a HeLa cell model using a neutral red assay and microscopy. The feasibility of using MgO for PDT was assessed. Empirical modelling was applied to corroborate the experimental results obtained from assessing cell viability losses and reactive oxygen species. The results indicate that MgO is an excellent candidate material for medical applications and could be utilized for its potential ability to upgrade conventionally used techniques.

Malignancy is considered to be the leading cause of long term injury, morbidity, and mortality worldwide[1]. Irrespective of the multidimensional treatment used, the blood–brain barrier is an obstacle to the recovery of neurological functions[2]. Surmounting this barrier is a key challenge that is being tackled by the design and implementation of transport mechanisms.

R.S. Kumaran investigated MgO nanoparticles (NP) with 20 nm size via the GST and ROS gene mechanism. The results showed that 150 µg/mL MgO nanoparticle dispersions liberate significant cytotoxins[3]. MgO NPs proved to be a promising material for biomedical applications due in cancer therapy, nano-cryosurgery, and hyperthermia. In addition MgO NPs enhanced ultrasound-induced lipid peroxidation in the liposomal membrane[4–6]. Magnetic resonance imaging (MRI) utilizes self-assembled multifunctional Fe/MgO for therapy. In addition, MgO is used extensively in research and clinical practice due to its various unique characteristics, including biocompatibility in correlating normal human *in vivo-in vitro* research, uptake in blood vessels without clotting, high bioavailability ratio for therapeutic purposes even at minimal concentrations as a contrast agent. Research results show that MgO-based contrast agents are ideal for use in MRI as a diagnostic and therapeutic material. Some surveys indicate that dynamic MgO enhancements for MRI purposes are more suitable for acute retroperitoneal fibrosis than chronic fibrosis. MgO also acts as a drug delivery and magnetic-activated cell storing vehicle.

It was previously reported that MgO NPs is supposed to be an auspicious materials due to its relevant biomedical applications, such as antibacterial/anticancer activity, magnetic hyperthermia, nano-cryosurgery, and as an MRI contrast agent[7–10].

[1]Institute of Fundamental and Frontier Science, University of Electronic Science and Technology of China, 610054, Chengdu, China. [2]Department of Physics, Government College University, 38000, Faisalabad, Pakistan. [3]Department of Physics and Astronomy, College of Science, King Saud University, Riyadh, Saudi Arabia. [4]National Institute of Laser and Optronics, Nilore, Islamabad, Pakistan. [5]Physics Department, Government College University (GCU), Lahore, Pakistan. [6]Department of Mathematics and Statistics, University of Lahore, Lahore, Pakistan. [7]Laser Spectroscopy Lab., Department of Physics, University of Agriculture Faisalabad, Faisalabad, Pakistan. [8]COMSATS Institute of Information Technology, Islamabad, Pakistan. Correspondence and requests for materials should be addressed to M.W.A. (email: waseem.physicist@gmail.com) or M.A. (email: atifhull@gmail.com) or Z.M.W. (email: zhmwang@gmail.com)

Though MgO NPs are being investigated as potential MRI contrast agents on a trial basis, Gadolinium (Gd) is also a candidate material for use in this area. Gd is a paramagnetic metal ion encapsulated with a chelating agent and is effective as a contrast agent in MRI. The use of chelating agents to improve the biodistribution of Gd towards specific target sites can lead to toxicity. The difference was very significant (mean 1.86, range 1.80–1.95 for acute, and mean 1.37, range 1.26–1.61 for chronic). Improved Gd-based MRI imaging can be achieved with Gd-based contrast agents (GBCAs) that have been approved by the FDA for improving bioavailability of drugs in body organs and tissues[11–13]. Magnesium-based oxide materials (e.g., MgO and $Mg(OH)_2$) are exceptional candidates as MRI contrast agents due to their extensive application in catalysis, superconductors, refractory materials, flame retardants, and paints[7,8,14]. A few reports illustrate results that have encouraged the development of various antimicrobial and drug-reactive NP materials (e.g., iron, gold, silver, zinc and manganese)[15–17]. It was recently reported that nano-MgO exhibits superior bactericidal, sporicidal, and antiviral activity in comparison compared with copper, silver, TiO_2, and various other bactericides[18–21]. Moreover, nano-MgO has significantly potent bactericidal effects under typical conditions and can be promptly prepared from economical solvents and precursors[22]. Electrostatic interactions between magnetic hybrid nano-carriers (e.g., dendrimer complexes) show morphological features that are desired in various biomedical applications, especially nucleic acid therapy. In this context, many experiments have successfully confirmed hybrid nano-carrier applications by analysis of zeta potentials, cell viability, cellular internalization, and lipid oxidation assays obtained using murine/human NIH/3T3 cells line or a mouse/human embryonic fibroblast cell model[23].

Simultaneous photodynamic/photothermal therapy (PDT/PTT) is more advantageous than peak-levelled lipid assembled combined chemotherapy because it is less invasive. The drug doxorubicin was shown to enhance the localization of the hybrid form of lipid NPs, leading to greater toxicity along with many beneficial effects[24].

Therefore, the introduction of inorganic nanomaterial oxide antimicrobial agents can improve neural functioning through advanced therapeutic modification. This paper presents the first report on the successful fabrication of polyvinyl-coated nano-sized MgO via chemical precipitation, which is considered to be a non-toxic, fast, economical, and environmentally benign methodology. Cellular responses to the novel NP materials were investigated in HeLa cell line.

Methods

Chemicals and Synthesis of MgO Nanotubes. Magnesium chloride ($MgCl_2$), sodium hydroxide (NaOH), polyvinyl alcohol (PVA), and ethanol were purchased from Sigma Aldrich and used as chemical reagents. Two transparent mixtures of $MgCl_2$ and NaOH were prepared separately in 50 ml of distilled water. A $MgCl_2$ mixture was slowly dripped in a NaOH solution (1:2) under constant stirring at 60 °C using a volumetric burette. This reaction process was completed within 1 h and held at room temperature for an additional hour to settle the milky suspension of magnesium hydroxide ($Mg(OH)_2$). This precursor was repetitively filtered and washed in water, followed by washing with ethanol in order to divest ions from the final product. The final product was vacuum dried at 60 °C overnight. The dried product was monitored using simultaneous TGA (thermogravimetry) and DSC (differential scanning calorimeter) analysis to identify the temperature where $Mg(OH)_2$ completely transforms into pure MgO. After thermal analysis, the dried powder was calcined at 450 °C for 2 h to achieve MgO nanopowder and was studied using diverse analysing tools. Beside this aforementioned process, there are many synthesis techniques that researchers have applied in different semiconductor devices and in studies on thermoelectric properties[25–29].

Characterization of Synthesized Nanopowder. The phase angle, crystal purity, and average crystallite size was determined using X-ray diffraction (XRD, PAN X' Pert PRO, Cu-Kα $\lambda = 1.5406$ Å). The morphology and particle size were measured using the JEOL 648OLV scanning electron microscope and JEM 1230 transmission electron microscope (a SEM and TEM, respectively). For TEM studies, MgO nanopowder was ultrasonically dispersed in acetone for 30 min. A few droplets of this solution were collected on a carbon-coated Cu grid and dried in vacuum. Elemental analysis was performed using an energy dispersive X-ray (EDX) analyser, while a SHIMADZU Prestige 21 Fournier transformation infrared (FTIR) spectrometer was operated between 300–600 cm^{-1} at room temperature to determine the molecular structure of the synthesized product.

Cell Cultures Conditions. *Cell Culturing and labelling condition.* The HeLa cell line was cultured and maintained at 37 °C in a 5% CO_2 humidified environment. Cells was grown in Dulbecco's modified Eagle's medium (DMEM) supplemented with 10% fetal bovine serum (FBS) during culturing and 2% FBS during experimentation. In addition, DMEM was supplemented with 1% Na-pyruvate and 1% nonessential amino acids. The solution was made with 5000 U/mL penicillin and 5000 mg/ml of streptomycin as antibiotics supplements. All growth media and supplements were purchased from Sigma-Aldrich.

Ethical Approval. All procedures regarding HeLa cell line culturing and maintenance were performed at China West Hospital (Huaxi Campus), Chengdu. All these experiments were performed in accordance with relevant guidelines and regulations identifying the institutional and/or licensing committee approving the experiments and experimental protocols. Finally, this procedure was approved by the institutional or licensing committee of IFFS-UESTC (Institute of Fundamental and Frontier Sciences, University of Electronic Science and Technology of China) to perform experiments on HeLa cell model.

Conjugation of MgO nanostructures with PEG and Fotolon. After successful growth of MgO nanostructures, stock solutions of dispersed NPs were prepared by mixing 10 mg/ml MgO NPs, 2 mg PEG (polyethylene glycol, Sigma Aldrich), and 10 mg/ml of chlorine e6 (Ce6, Fotolon). The mixture was stirred for 30 min at 27 °C. After successfully preparing the working solutions of PEG-coated MgO NPs or PEG-coated MgO NPs with Fotolon,

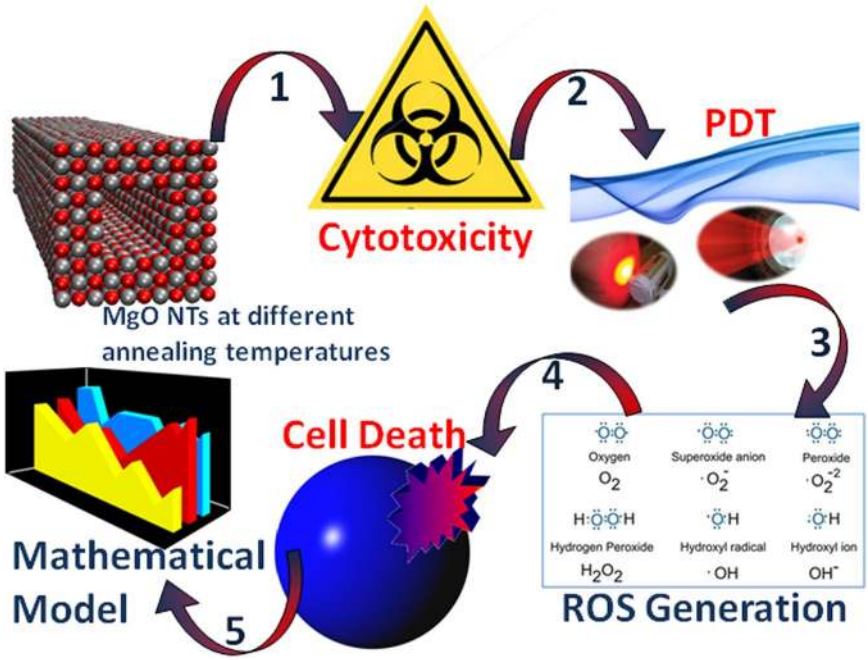

Figure 1. Schematic illustration of MgO based PDT by manifold techniques.

a previously published procedure was applied to obtain MgO NPs of different morphologies using a variety of annealing temperatures[30–32]. Cell uptake was measured using a microplate reader at various incubation times, and cell viability was assessed using the MTT assay as described below.

MTT Assay. The experimental scheme for cell labelling used 96 well plates for sub-culturing and experimentation, as follows. In Group I, five wells in each row received increasing concentrations of MgO NPs dispersed in solution (0–400 µg/ml). The last two columns were used as controls, i.e., without treatment. In group II, PEG-coated MgO nanostructures complexed with Fotolon were exposed to HeLa cells to assess their physiochemical response to the prepared solution (original and annealed form of MgO nanostructures). In Group III, the same experimental procedure was repeated, albeit with the addition exposure to 10–80 J/cm^2 laser light at 660 nm wavelength. The incubation times for cell localization were 6, 24, and 48 h. The viability of each well was assessed using the MTT assay[33,34].

ROS analysis. The production of intracellular reactive oxygen species (ROS) was measured using the non-fluorescent compound CM-H_2DCFDA (2,7-dichlorodihydrofluorescein diacetate acetyl ester; Invitrogen Co., USA). This compound crosses the cell membrane and undergoes deacetylation by an esterase, producing non-fluorescent CM-H_2DCF. HeLa cells were seeded in a black 96-well plate and incubated in the presence of different MgO concentrations or MgO + Fotolon (0–400 µg/ml) for 14 h in darkness and 5% CO_2 humidified air at 37 °C. Parallel steps were performed for the working MgO suspension in darkness, as well as with a suitable dose of 660 nm of laser radiation.

After experimentation, the cells were gently washed in DMEM. Cells loaded with 100 µL of 5 µM CMH_2DCFDA were incubated for 30 min at 37 °C and protected from light.

Thereafter, the cells were exposed to an optimal built-in microscopic light dose of 10 J/cm^2 for 2 min and were then assessed for ROS fluorescence using a Wallac 1420 Victor Plate Reader (λ_{ex} 485/λ_{em} 530 nm). Cells were also cultured in Petri dishes treated as above and were excited using blue light (488 nm), thus making them ready for microscopic imaging[35,36]. In addition, the immunofluorescence test was performed following assay.

Results

Figure 1 shows a schematic illustration of MgO-based photodynamic therapy by manifold analysis. Toxicity was measured in both light and dark conditions and verified with a mathematical model.

Figure 2 shows the XRD pattern of the MgO NPs sintered at 900 °C for 6 h. The seven prominent peaks that appear in the XRD pattern show a single phase crystalline structure. The Miller indices labelled on the peaks were determined using JD computer software. The lattice parameter was calculated using the formula:

$$a = \frac{\lambda}{2\sin\theta}\sqrt{h^2 + k^2 + l^2} \quad (1)$$

The value of the obtained lattice parameter was 8.3083 Å, while the unit cell volume was found by using the value of the lattice parameter $b = a^3$ in a cubic unit cell Moreover, the crystal size was calculated using the Scherer formula:

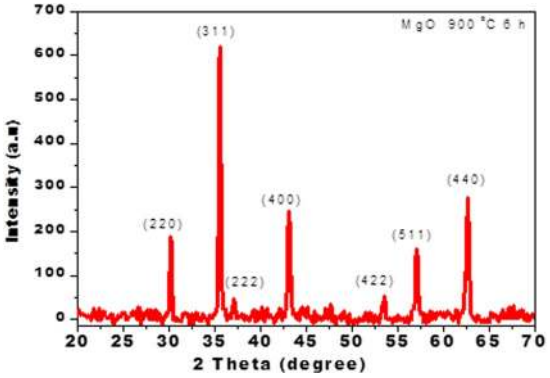

Figure 2. XRD pattern of MgO nanoparticles.

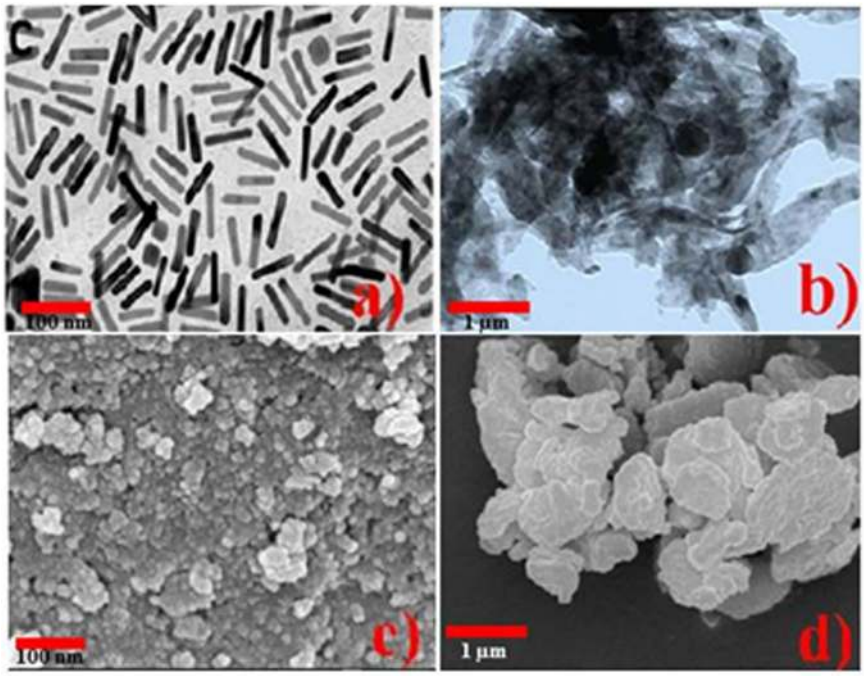

Figure 3. TEM images of various-shaped MgO nanorods (**a**) TEM of MgO nanotubes, scale bar = 100 nm, (**b**) TEM of MgO nanoflakes, scale bar = 1 µm, (**c**) MgO NPs Scale bar: 100 nm, and (**d**) SEM of MgO nanoflakes, scale bar = 1 µm.

$$D = \frac{0.9\lambda}{b\cos\alpha} \tag{2}$$

0.9 is the shape factor, λ is the wavelength of the copper alpha source, and βθ is the full width half wavelength. θ is diffraction angle measured in radians. The average size of the MgO NPs was 53 nm. The sharp XRD peak in the 1–1 plane showed that the synthesized material had grown to a crystal size of 60.60 nm.

Figure 3 shows the results of morphological analysis of the nanomaterials using TEM (a-b) and SEM (c-d). The prior results were confirmed using TEM images of MgO nanorods (MgO NRs) and MgO nanotubes (MgO NTbs). In these samples, the scale bar was set to 100 nm, and a nanorod morphology of 12 nm diameter and about 80 nm length is shown in Fig. 3(a). Figure 3(a) shows TEM images of MgO NTbs with 16–25 nm length, where the scale bar is 100 nm. Figure 3(b) shows TEM images, where the scale bar is 100 nm. Figure 3(c) shows an SEM image of the MgO NPs, where the scale bar is 100 nm. Figure 3(d) shows an SEM image of the MgO NFKs with 200–500 nm length, where the scale bar is 1 µm.

Fourier transform infrared spectroscopy (FTIR). FTIR spectra were measured using a NICOLET 6700 FT-IR system. The data shows the following dominant peaks in transmission mode. The first peak lies at 500 cm^{-1}, which corresponds to MgO. The second significant peak relevant to carbon appears at approximately 1491 cm^{-1}. The third and last dominant transmittance peak lies at 3575 cm^{-1}, indicating that Mg exhibits a O-H group, as

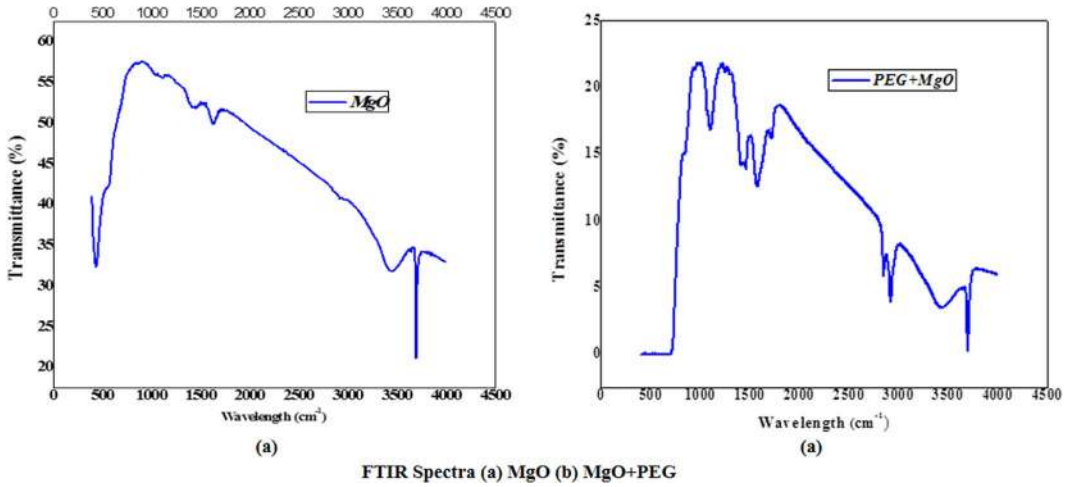

Figure 4. FTIR spectra from (**a**) MgO; (**b**) PEG + MgO.

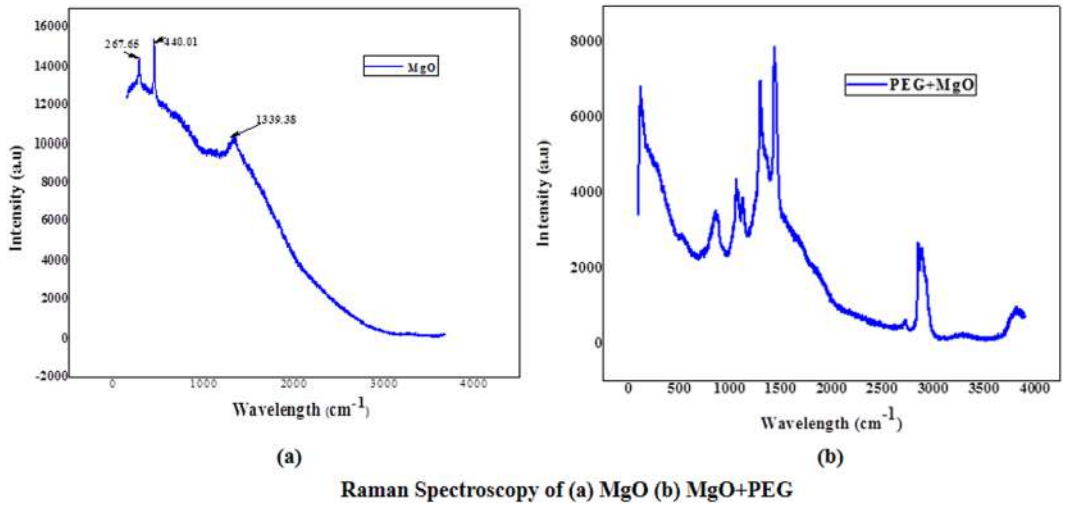

Figure 5. Raman spectroscopy from (**a**) MgO (**b**) MgO + PEG.

shown in Fig. 4(a). In Fig. 4(b), the dominant peaks are 1103 cm^{-1} and 1246 cm^{-1}, and the data shows the presence of an amide carbonyl bond (O=CNH) at 1615 cm^{-1}. This suggests conjugation of PEG. Another peak at 3810 cm^{-1} indicates strong bonding with Mg and strong absorption corresponds to stretching of H-O bonded with Mg.

Raman Spectroscopy. The dominant peaks in MgO are shown in Fig. 5(a). The Raman spectra were gathered in the 50–4000 cm^{-1} range.

Raman Spectrum MgO + PEG. The adsorption of Polyethylene Glycol (PEG) on the surface of MgO plays a key role in drug delivery towards a targeted site or tumour. In this experimental scheme, PEG-coated MgO conjugated with efficient photosensitizers were employed for cancer tissue island necrosis via ROS. The Raman spectrum of MgO + PEG is shown in Fig. 5(b). The presented band locations indicate enlarging vibrations of the CH triple bond chain observed at 3000 cm^{-1}. The bands at 1478 and 1442 cm^{-1} are assigned to the bending mode of the hydrocarbon group. The bands appearing at 1180 and 1125 cm^{-1} correspond to twisted vibrations in C-H. A peak appearing at 450 cm^{-1} can be attributed to Mg. All of the experiments were performed at room temperature.

Thermal Analysis of MgO and PEG coated MgO. The thermal degradation behaviour of MgO and pegylated MgO is shown in Fig. (6a). 4 wt. % loss occurred at temperatures ranging from 180 °C to 200 °C, due to the loss of imbibed solvent molecules. Significant weight loss and polymer polyethylene glycol degradation in PEG-coated MgO were recorded as an initial weight loss of about 48% as temperature rose from 300 °C to 500 °C. Weight loss of about 9% was observed as the temperature rose from 500 °C to 768 °C. The energy loss curve at 350 °C to 450 °C showed that weight loss occurred in PEG-coated MgO, as shown in Fig. 6(b). All data were collected with a Perkin Elmer Diamond TG/DT Analyzer with the Pyris Manager built-in software.

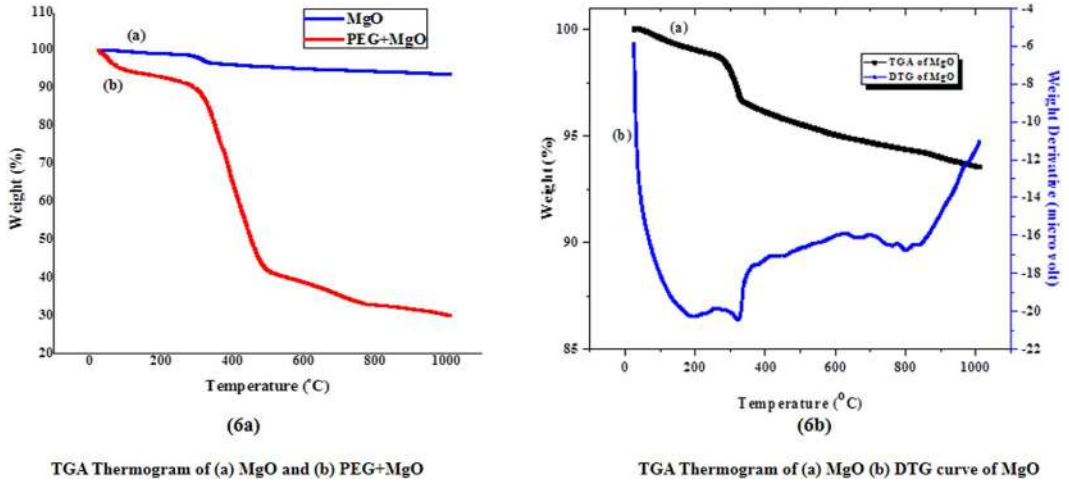

Figure 6. TGA thermogram of (a) MgO and (b) PEG + MgO. TGA Thermogram of (c) MgO (d) DTG curve of MgO.

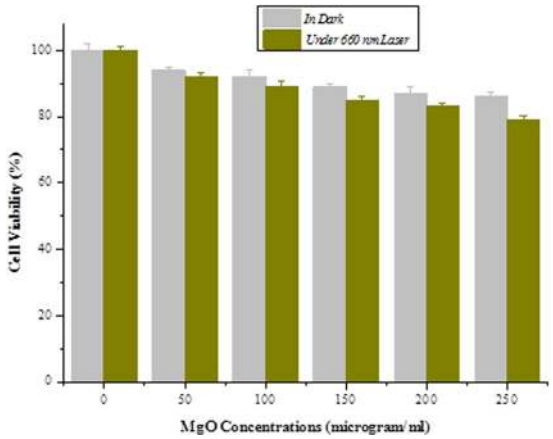

Figure 7. Cell viability loss in HeLa cell line exposed to MgO nanotubes in the dark and with 660 nm laser irradiation.

Figure 7 shows the cell viability loss in dark conditions, as well as with a dose of 660 nm laser light. First, the MgO nanotube concentration and light dose were optimized (250 µg/ml and 80 J/cm^2, respectively)[37,38]. In the final investigation, superficial cell viability loss of approximately 14% was observed in the cell line labelled with 250 µg/ml MgO dispersed in dark conditions. The cell viability loss reached 21% under the same experimental conditions with 660 nm of laser exposure. We suspect that MgO is not too toxic for applications as a candidate for disease or cancer diagnosis, especially in the biomedical fields. In many other studies, results indicated that MgO nanomaterials are less toxic due to their smooth morphology, which reflects that the toxicity of nanomaterials is morphology and size/concentration dependent[3,39]. Cell viability is dependent on MgO concentration in experiments conducted in darkness and with 660 nm laser light. The loss of cell viability can be expressed using a second order polynomial model, as shown in Eq. (3). The values of the polynomial constants are described in Table 1. The mathematical model and its validity is described in the mathematical model section.

It worthy of note that the cell viability under illumination with 660 nm laser light showed a larger decrease with increasing MgO concentration compared to dark conditions, as shown in Fig. 8. For further investigation regarding the chemical toxicity signature of MgO, four different *in vitro* samples were exposed to the same concentration of solutions with different MgO morphologies (0–250 mg/ml). No obvious toxicity or significant difference between the different MgO nanostructures was identified by using MTT assay (Fig. 9). The dose dependence of cellular survival effects was determined by applying MgO NTs, NRs, NSPs, and NSTs, each corresponding to 79%, 85%, 85%, and 83% cell viability, respectively. Cell viability remained more than 78% in every case after administration of a suitable concentration of MgO nanostructures (≈250 mg/ml) in the cell model. After summarizing the cytotoxicity results, we are of the opinion that MgO would be useful for MRI applications and for reliable drug delivery protocols with the benefit of low toxic effects in a cell model. The same type of experimental study was reported in previously published research[40–43].

	P_1	P_2	P_3	SSE	R-square	Adjusted R-square	RMSE	P-value
$Model_1$	0.0001786	−0.09836	99.54	1.664	0.9877	0.9795	0.7448	0.0001
$Model_2$	0.0001714	−0.1206	99.14	4.914	0.9822	0.9703	1.28	0.0001
$Model_3$	0.0001714	−0.1206	99.14	4.914	0.9822	0.9703	0.3342	0.0001
$Model_4$	0.0002214	−0.1136	99.46	3.264	0.98	0.9667	1.043	0.0002
$Model_5$	0.0002857	−0.1269	99.14	5.371	0.9662	0.9436	1.338	0.0004
$Model_6$	0.0001786	−0.1081	99.25	3.379	0.9819	0.9699	1.061	0.0001

Table 1. Values of different constants used in the model given in Eq. (3) and indicators of curve fitness. $Model_1$ = In Dark; $Model_2$ = Under laser; $Model_3$ = MgO NRs; $Model_4$ = MgO NP; $Model_5$ = MgO NFKs; $Model_6$ = MgO NFTs.

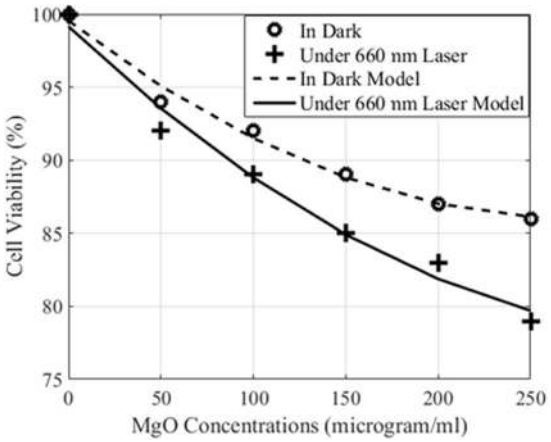

Figure 8. Comparison of experimental and modelled cell viability loss in the dark and with 660 nm irradiation.

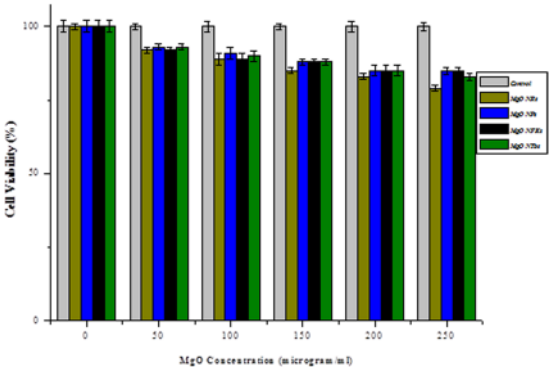

Figure 9. Cell viability loss in HeLa cell line exposed to MgO nanotubes dispersed in darkness or with 660 nm laser irradiation.

Four different experiments were simulated using our mathematical model (Fig. 10). All the experimental data was analysed using the least squares method, followed by a mathematical expression. It was observed that the best model that fit all of the curves is the 2nd order polynomial, as the sum of the square of errors is lower for this polynomial. Lower order polynomial produce larger error. The model presented in Eq. (3) produced errors of less than 5%, which is sufficient to validate the experimental data. It was also observed that the cell viability decreased with increasing MgO concentration. The rate of decrease in cell viability was maximal for the MgO NR's as opposed to the other morphological varieties and was modelled with suitable constants provided by the above equations. All other experiments were similarly analysed, as shown in Fig. 10.

ROS Detection. HeLa cells were seeded in a black 96-well plate and incubated at different MgO or MgO + Fotolon concentrations (0–400 µg/ml) in 5% CO_2 humidified air at 37 °C. The incubation time was set to 14 h, and cells were incubated in total darkness or after receiving a suitable dose of 660 nm laser radiation.

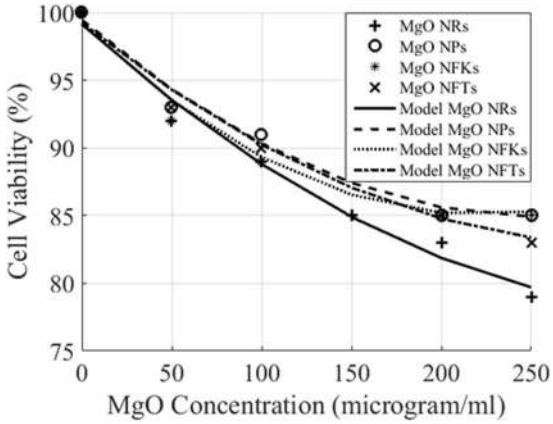

Figure 10. Comparison of experimental and modelled cellular viability loss with its mathematical.

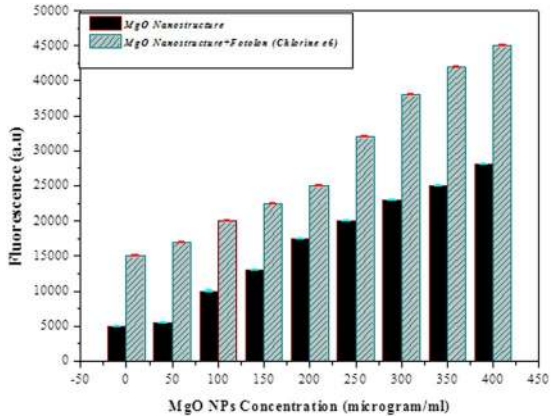

Figure 11. ROS Fluorescence micrographs for *in vitro* HeLa cells.

After experimentation, the cells were incubated with CMH_2DCFDA for ROS detection (Fig. 11 (micrograph) and Fig. 12 (ROS snapshot)). Significant ROS levels were observed when HeLa cells were exposed to a suitable concentration (μg/ml) of PEG-coated MgO + Fotolon under laser exposure. In the case of PEG + MgO in the absence of laser irradiation, measured changes were superficial.

The fluorescence values were dependent on MgO NPs concentration levels. The trend suggests that it can be modelled with a linear function. The values for the slopes and y-intercepts were calculated using the least squares method. One can see that the slope for the MgO NPs was less than the slope of MgO + Fotolon, which shows that the MgO + Fotolon has a higher effect on fluorescence than MgO NPs. The proposed mathematical model is described in the following section, and a comparison of math model with the original data is shown in Fig. 13.

Mathematical Model. Based on the measured data, a mathematical model is proposed which maps the original data to the 2nd order polynomial with reasonably lower percentage error. Mathematical model is shown in Eq. (3). The model shown in Eq. (3) is fit using regression. Figures 8 and 10 show a comparison between the proposed model with the experimental data. One can see that the proposed model agrees well with the experimental data. This is highlighted with different figures of merit shown in Table 1 (SSE, R-square, Adjusted R-Square, RMSE, and P-values). All of the values shown in Table 1 confirm the applicability of the model with reasonably low percentage error.

$$Model_i = P_1x^2 + P_2x + P_3 \tag{3}$$

$Model_i$ has six possibilities, as shown in the Figs 7 and 9 (i = {1, 2, 3, 4, 5, 6}). x is the MgO concentration, and P_1, P_2, and P_3 are extracted from the fitting procedure and are shown in Table 1.

The mathematical model for fluorescence (a.u) is shown in Fig. 13. The fluorescence is shown with respect to changes in MgO NP concentration and is also fit using linear regression. One can see that there is a linear relationship, which implies a linear model. The proposed linear model is shown in Eq. (4).

$$Model_i = P_1x + P_2 \tag{4}$$

where $Model_i$ has two options, as shown in the Figs. 11 (i={7, 8}). x is the MgO NP concentration, and P_1 and P_2 are extracted from the fitting procedure and are shown in Table 2.

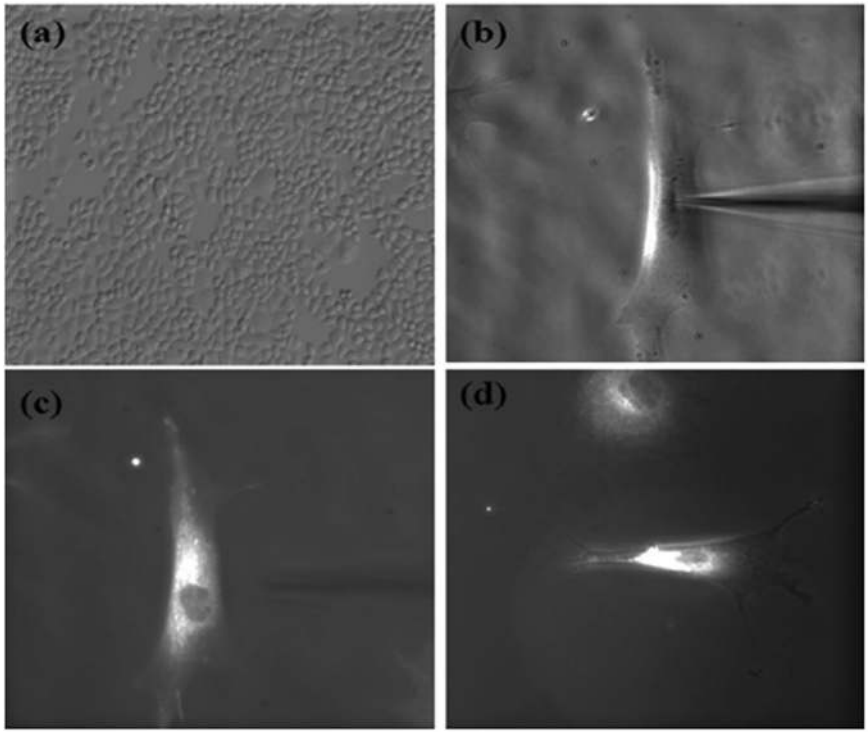

Figure 12. ROS Fluorescence images of *in vitro* HeLa cells after exposure to PEG-coated MgO + Fotolon via intravenal injection after laser irradiation. (**a**) Control HeLa cells. (**b**) Snapshot during microinjection. (**c**) After 10 min of drug delivery. (**d**) ROS production image.

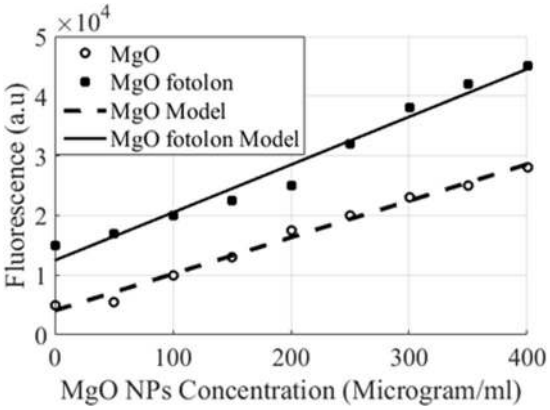

Figure 13. Comparison of experimental and modelled fluorescence ROS micrographs.

	P_1	P_2	SSE	R-square	Adjusted R-square	RMSE	P-value
$Model_7$	61.27	4069	6.635e + 0	0.9884	0.9867	973.6	0.0001
$Model_8$	80.17	1.247e + 04	2.8e + 07	0.9718	0.9677	2000	0.0002

Table 2. Values of different constants used in the model given in Eq. (4) and indicators of curve fitness. $Model_7$ = MgO; $Model_8$ = MgO Fotolon.

Conclusion

A co-precipitation technique was used to grow MgO nanostructures with various morphologies. MgO nanorods (12 nm diameter and ~80 nm length), MgO NTbs (16–25 nm length), NPs, and MgO NFKs (200 nm to 500 nm in size) were grown using the co-precipitation process. TEM and SEM results confirm symmetric and asymmetric forms of the nanostructures in both an individual and agglomerated manner for the different nanomaterials. The results confirmed the noxious effects of these materials, where a 17% loss in cell viability was observed in the MTT assay. In addition, the biotoxicity increases as long as heat treatment towards nanomaterials increases the

permeability of nanoparticle enhancement. Therefore, cell viability was significantly less with treatment at 550 °C compared to 450 °C. An empirical model was applied to assess the validity of the experimental results, where the modelling results were in good agreement with the experimental results. However, more careful assessments are required for therapeutic purposes.

References

1. Silverman, E. *et al*. An atlas of investigation and treatment: Ischemic stroke. *Atlas Medical Publishing Ltd.* **13**, 978 (2009).
2. Bhaskar, S. *et al*. Multifunctional nanocarriers for diagnostics, drug delivery and targeted treatment across blood-brain barrier: perspectives on tracking and neuroimaging. *Part. Fibre Toxicol.* **7**, 25 (2010).
3. Kumaran, R. S. *et al*. *In vitro* cytotoxic evaluation of MgO nanoparticles and their effect on the expression of ROS genes. *Int. J. Mol. Sci.* **16**(4), 7551–7564 (2015).
4. Krishnamoorthy, K. *et al*. Mechanistic investigation on the toxicity of MgO nanoparticles toward cancer cells. *J. Mat. Chem.* **22**(47), 24610–24617 (2012).
5. Ge *et al*. Cytotoxic effects of MgO nanoparticles on human umbilical vein endothelial cells *in vitro*. *IET Nanobiotechnol.* **5**, 36–40 (2011).
6. Sun, J. *et al*. Cytotoxicity, permeability, and inflammation of metal oxide nanoparticles in human cardiac microvascular endothelial cells. *Cell Biol. Toxicol.* **27**, 333–342 (2011).
7. Krishnamoorthy *et al*. Antibacterial activity of MgO nanoparticles based on lipid peroxidation by oxygen vacancy. *J. Nanopart. Res.* **14**, 1063 (2012).
8. Boubeta, M. *et al*. Self-Assembled Multifunctional Fe/MgO Nanospheres for Magnetic Resonance Imaging and Hyperthermia. *Nanomedicine: Nanotechnology, Biology and Medicine* **6**, 362–370 (2010).
9. Chalkidou, A. *et al*. *In vitro* application of Fe/MgO nanoparticles as magnetically mediated hyperthermia agents for cancer treatment. *J. Magn. Mater.* **6**, 775–780 (2011).
10. Di, D. R., He, Z. Z., Sun, Z. Q. & Liu, J. A new nano-cryosurgical modality for tumor treatment using biodegradable MgO nanoparticles. *Nanomedicine: Nanotechnology, Biology and Medicine* **8**, 1233–1241 (2012).
11. Broome, D. R. *et al*. Gadodiamide-associated nephrogenic systemic fibrosis: why radiologists should be concerned. *AJR Am. J. Roentgenol.* **188**, 586–592 (2007).
12. Kanal, E. *et al*. ACR guidance document for safe MR practices. *AJR Am. J. Roentgenol.* **188**, 1447–1474 (2007).
13. Kuo, P. H. *et al*. Gadolinium-based MR contrast agents and nephrogenic systemic fibrosis. *Radiology* **242**, 647–649 (2007).
14. Jintakosol, T. & Singjai, P. Effect of annealing treatment on luminescence property of MgO nanowires. *Curr. Appl. Phys.* **9**, 1288–1292 (2009).
15. Duan, G. *et al*. Nanosized CuO–ZrxCe1− xOy aerogel catalysts prepared by ethanol supercritical drying for catalytic deep oxidation of benzene. *Powder Technol.* **194**, 109–114 (2007).
16. Niu, H. *et al*. Selfassembly of porous MgO nanoparticles into coral-like microcrystals. *Scr. Mater.* **54**, 1791 (2006).
17. Fakhar-e-Alam, M. *et al*. Empirical modeling of physiochemical immune response of multilayer zinc oxide nanomaterials under uv exposure to melanoma and foreskin fibroblast. *Sci. Rep.* **7**, 46603 (2017).
18. Fresta, M. *et al*. Preparation of nanoparticles consisting of methacrylic polymers and drugs by an aerosol flow reactor method. *J. Pharm. Sci.* **84**, 895 (1995).
19. Forestier, F. *et al*. Effect of nanoparticle-bound ampicillin on the survival of Listeria monocytogenes in mouse peritoneal macrophages. *J. Antimicrob. Chemother.* **30**, 173–179 (1992).
20. Cui, Z. *et al*. Preparation and characterization of MgO nanorods. *Materials Research Bulletin* **35**, 1653–1659 (2000).
21. Kim, H. W. *et al*. Nanosized materials because of their unusual physical, chemical and mechanical properties. *J. Korean Phys. Soc.* **49**, 628 (2006).
22. Stoimenov, P. K. *et al*. Metal oxide nanoparticles as bactericidal agents. *Langmuir* **18**, 6679 (2002).
23. John, J. V. *et al*. Polymer-block-polypeptides and polymer-conjugated hybrid materials as stimuli-responsive nanocarriers for biomedical applications. *J. Biomed. Nanotechn.* **11**, 1–39 (2015).
24. Ma, W. *et al*. Biodegradable core-shell copolymer-phospholipid nanoparticles for combination chemotherapy: an *in vitro* study. *J. Biomed. Nanotech.* **11**, 1193–1200 (2015).
25. Wenchao, W. *et al*. Green preparation of Au nanoparticles for electrochemical detection of H_2O_2. *J. Semicond* **37**, 1 (2016).
26. Cuiyue, F. *et al*. Investigation of aluminum gate CMP in a novel alkaline solution. *J. Semicond.* **37**, 1 (2016).
27. Jantrasee, S., Moontragoon, P. & Pinitsoontorn, S. Thermoelectric properties of Al-doped ZnO: experiment and simulation. *J. Semicond.* **37**, 9 (2016).
28. Kun *et al*. High-quality ZnO growth, doping, and polarization effect. *J. Semicond.* **37**, 3 (2016).
29. Takahashi, M. *et al*. Catalyst-free growth of ZnO nanowires on various-oriented sapphire substrates by pulsed-laser deposition. *J. Semicond.* **37**, 2 (2016).
30. Peng, J. *et al*. Mesoporous magnetic gold "nanoclusters" as theranostic carrier for chemo-photothermal co-therapy of breast cancer. *Theranostics* **4**, 678–692 (2014).
31. Liao, J. *et al*. Combined cancer photothermal-chemotherapy based on doxorubicin/gold nanorod-loaded polymersomes. *Theranostics* **5**, 345–356 (2015).
32. Makhluf, S. *et al*. Microwave-Assisted synthesis of nanocrystallinemgo and its use as a bacteriocide. *Adv. Funct. Mater.* **15**, 1708–1715 (2005).
33. Shah, M. A. & Qurashi, A. H. Novel surfactant-free synthesis of MgOnanoflakes. *J. Alloys Compd.* **482**, 548–551 (2009).
34. Butt, A. R., Ejaz, S., Baron, J. C., Ikram, M. & Ali, S. CaO nanoparticles as a potential drug delivery agent for biomedical applications. *Dig. J. Nanomater. Biostruct.* **10**, 799–809 (2015).
35. Ejaz, S. *et al*. Characterizing infarction and selective neuronal loss following temporary focal cerebral ischemia in the rat: a multi-modality imaging study. *Neurobiol. Dis.* **51**, 120–132 (2013).
36. Bonvin, D. *et al*. Tuning Properties of Iron Oxide Nanoparticles in Aqueous Synthesis without Ligands to Improve MRI Relaxivity and SAR. *Nanomater.* **7**, 225 (2017).
37. Xiao, S. *et al*. PAMAM Dendrimer/pDNA functionalized-magnetic iron oxide nanoparticles for gene delivery. *J. Biomed. Nanotechnol.* **11**(8), 1370–1384 (2015).
38. Xu, H. *et al*. Self-assembled monomethoxy (polyethylene glycol)-b-P(D,L-Lactic-co-glycolic acid)-b-P(L-glutamic acid) hybrid-core nanoparticles for intracellular pH-triggered release of doxorubicin. *J. Biomed. Nanotechnol.* **11**(8), 1354–1369 (2015).
39. Ge, S. *et al*. Cytotoxic effects of MgO nanoparticles on human umbilical vein endothelial cells *in vitro*. *IET Nanobiotechnol.* **5**(2), 36 (2011).
40. Alam, M. F. *et al*. Pharmacokinetics and biodistribution of nickel oxide for liver cancer cure. *J. Optoelectron. Adv. Mat.* **18**, 414–418 (2015).
41. Alam, M. F. *et al*. ZnO Nanoparticles as drug delivery agent for photodynamic therapy. *Laser Phys. Lett.* **11**, 025601 (2014).
42. Alam, M. F., Kishwer, S. & Willander, M. Photodynamic effects of zinc oxide nanowires in skin cancer and fibroblast. *Laser Med. Sci.* **29**, 1189–1194 (2014).
43. Betzer, O. *et al*. *In vitro* optimization of nanoparticle-cell labeling protocols for *in vivo* cell tracking applications. *Sci. Rep.* **5**, 15400 (2015).

Acknowledgements
The author would like to acknowledge the Higher Education Commission, Pakistan for financial support through IRSIP. The authors would like to extend their sincere appreciation to the Deanship of Scientific Research at King Saud University for its funding of this research through the Research Group Project No. RGP-VPP-293.

Author Contributions
Experiment Design: Muhammad Waseem Akram, Dr. Muhammad Atif. Experiment Performed: Muhammad Waseem Akram, Dr. Yasir Jamil Statistics and Empirical Modelling: Dr. Khuram Saleem Alimgeer, Ali Asghar Paper writing: Muhammad Waseem Akram, Dr. Muhammad Fakhar-e-Alam Valuable discussion: Prof. Zhiming M. Wang, Prof. Muhammad Atif Image taken: Dr. Muhammad Fakhar-e-Alam, Muhammad Waseem Akram, Alvina Rafique Butt.

Additional Information
Competing Interests: The authors declare no competing interests.

Publisher's note: Springer Nature remains neutral with regard to jurisdictional claims in published maps and institutional affiliations.